



Ice crystal number concentration from measurements of lidar, cloud radar and radar wind profiler

Johannes Bühl¹, Patric Seifert¹, Martin Radenz¹, Holger Baars¹, and Albert Ansmann¹

¹Leibniz Institute for Tropospheric Research, Permoserstr. 15, 04318 Leipzig, Germany

Correspondence: Johannes Bühl (buehl@tropos.de)

Abstract. A new method for the retrieval of ice particle number concentrations from combined active remote-sensing measurements of Raman lidar, cloud radar and radar wind profiler is presented. We exploit – for the first time – measurements of terminal fall velocity together with radar reflectivity factor and/or lidar-derived particle extinction coefficient in clouds for retrieving the number concentration of pristine ice particles with presumed particle shapes. A lookup table approach for the retrieval of the properties of the particle size distribution from observed parameters is presented. Analysis of methodological uncertainties and error propagation are performed, which shows that a retrieval of ice particle number concentration is possible within the order of magnitude. Comparison between a retrieval of number concentration based on terminal fall velocity on the one hand and lidar and cloud radar on the other shows agreement within the uncertainties of the retrieval.

1 Introduction

10 Aerosols, clouds and precipitation are major components of Earth's climate system. The complex aerosol-cloud-dynamics interaction currently poses major challenges for numerical modeling of climate and weather phenomena because the majority of rain formation on Earth happens through the ice phase (Mülmenstädt et al., 2015). The process of heterogeneous ice nucleation in clouds is of particular importance because it constitutes the link between aerosol conditions – including ice nucleating particle concentration (INPC) – and precipitation formation. An understanding of ice nucleation and growth is necessary for understanding precipitation formation, cloud stability (Korolev et al., 2017), secondary ice formation (Sullivan et al., 2017), and cloud radiative transfer (Sun and Shine, 1994). It is, hence, a key process for the global weather and climate system which must be understood in detail in order to make accurate predictions about cloud and precipitation patterns in state-of-the-art numerical weather forecast and future climate projections.

Up to date, ice nucleation cannot be observed directly in the atmosphere, but we are gaining the ability to retrieve ice crystal number concentration (ICNC, furtherly designated N) and the respective ice crystal number flux (F) are a promising approach to gain quantitative information about ice nucleation in clouds. Apart from N , $F = N \times v_t$ (with v_t the terminal fall velocity) is especially well suited to derive the rate of ice production in clouds. An illustration of the use of F in comparison with N is given in Fig. 1. F of falling ice particles yields a direct measure of the rate of ice production in the cloud above. Bühl et al. (2016) estimated ice mass fluxes produced in well-constrained shallow stratiform cloud layers. Based on these measurements, information about the contribution of ice precipitation on the mass balance of the mixed-phase cloud layer was retrieved.



Aircraft observations have been used frequently for measuring N and F via optical measurement of the particle size distribution (PSD) of ice crystals (Eidhammer et al., 2010; Westbrook and Illingworth, 2013; Voigt et al., 2017). Such observations can indeed deliver a quantitative picture of N and the shape of particles, but since they take place at only one height level, the actual level of ice formation is often not known and blurring the resulting long-term statistics. Ground-based remote sensing provides accurate information about the ice nucleation level, however, retrieving N from remote sensing measurements is extremely challenging. Especially, freshly created pristine ice crystals pose challenges in this context because they vary strongly in shape over different ranges of ice nucleation temperature which sensitively influences the accuracy of retrievals and model results (Simmel et al., 2015).

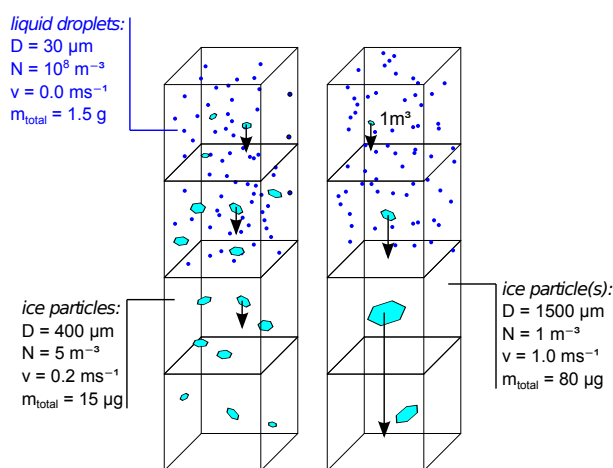


Figure 1. Comparison of two clouds with different ice crystal number concentrations N but with the same ice crystal number flux $F = 1 \text{ m}^{-2} \text{ s}^{-1}$ ($F = N \times v_t$ with v_t terminal fall velocity) and, hence, also the same rate of ice production: (a) Higher ice crystal number concentration (N) but less total ice mass and (b) lower N and higher total ice mass.

Today, all remote-sensing approaches for retrieving N need a priori information about crystal size before being able to derive N . Extensive observational variables like lidar-derived optical particle extinction E or radar reflectivity factor Z can then be used to retrieve N . Hence, the task of deriving an estimation of particle size is central for deriving N . Different methods exist for retrieving information about particle size. Ceccaldi et al. (2013) and Sourdeval et al. (2018) employ a forward iteration method in order to obtain an estimation of N from combined observations of spaceborne lidar and cloud radar. An estimation of N based on assumptions (e.g., on particle shape) is possible with this technique if both lidar and cloud radar (CR; Görndorf et al. (2015)) observations are available. This method exploits the strong wavelength dependence in the efficiency of backscatter signal between lidar (geometrical scattering) and radar (Rayleigh/Mie scattering) for ice particles. In optically thick clouds, where only CR measurements are available, the method falls back to parameterizations of particle size and retrieval of N is no longer possible. Also multi-frequency radar observations have been introduced for measurement of particle sizes (Battaglia et al., 2014; Sekelsky et al., 1999; Kneifel et al., 2011). However, such methods do not work for small pristine particles



(diameter smaller than about 1 mm, Battaglia et al. (2014)). For these particles, only the terminal fall velocity v_t leaves traces about particle size, but actual observations of v_t are difficult to obtain. Such observations have been made in laboratories (Fukuta and Takahashi, 1999) and, recently, Bühl et al. (2015) and Radenz et al. (2018) showed that a combinations of CR and radar wind profiler (RWP; Steinhagen et al. (1998); Lehmann and Teschke (2001)) can be used in order to derive v_t of ice particles.

In the present work, we make use of these new measurements and present an alternative approach for retrieval of N that works in the presence of very small pristine ice crystals and in clouds which cannot be penetrated by lidar. v_t and spectral width w obtained from combined Doppler spectra observed with CR and RWP are used to derive median Diameter (D_m) and the shape parameter μ of a modified gamma distribution. This kind of distribution was described by Delanoë et al. (2005) as universally applicable for ice crystal populations. A forward model approach based on a lookup table of numerically derived microphysical and observed parameters is employed in the present work. Combinations of environmental and microphysical input parameters are used to compute a lookup table with a set of observable variables, e.g., v_t , optical extinction (E) and Z . The observable variables are compared to the actually measured variables in order to come up with an estimation of ice crystal properties, F and N .

The paper is structured as follows. Section 2 describes how the data used in the paper has been acquired. In Section 3 the method for deriving information about the particle size distribution from both v_t and combined lidar/radar measurements is described. Section 4 presents example case studies. Conclusion and outlook are given in Section 5.

2 Data

The remote-sensing data used in the context of this work was acquired during the COLRAWI-2 campaign (Combined observations with lidar radar and wind profiler) at Richard-Aßmann-Observatory (RAO) of DWD in Lindenberg, Germany between 1 June 2015 and 30 September 2015 (Bühl et al., 2015). Figure 2 shows a case study of the combined measurements at Lindenberg. During the project, an ultra-high frequency (UHF) RWP was used to measure the vertical velocity of air (v_{air}) in combination with measurements of Z , mean Doppler velocity v_D and spectral width w with a vertically pointing 35-GHz CR. The RWP was switching between vertically pointing and horizontal beam swinging each 30 min. This special observation mode of the RWP was necessary to acquire direct measurements of both horizontal and vertical air motions with only one RWP available. A Polly^{XT} Raman lidar (Engelmann et al., 2016) pointing 5° off zenith was used for measurement of ice particle extinction coefficient (E) which is derived at a wavelength of 1064 nm (Baars et al., 2017). For the sake of completeness also a Streamline XR Doppler lidar (Päschke et al., 2015) should be mentioned which was also observing vertical Doppler velocity v_{DL} . However, its measurements are left out of the retrieval method, because they (a) provide mainly redundant information to the cloud radar and (b) pose additional problems in interpretation of optical signals due to specular reflection at orientated ice crystals.

A Cloudnet (Illingworth et al., 2007) dataset was derived from the lidar/CR/MWR measurements including the attenuation corrected values of CR reflectivity used in this paper. The combined measurements of CR and RWP were used to derive a



dataset of particle ensemble mean v_t with an error margin of about 0.1 ms^{-1} (Radenz et al., 2018). It is worth noting here that in the context of this work we use “uncertainty” to describe retrieval and methodological uncertainties and “errors” for measurement errors. This unique dataset is used here for the first time to test the retrieval method and give examples.

3 Methods

5 3.1 Measuring terminal fall velocity

The retrieval presented in this paper is based on measurements of radar reflectivity factor Z and terminal fall velocity v_t with CR and RWP. Measuring Z and v_t of ice particles in clouds is difficult because different factors influence the CR Doppler spectrum of ice particles:

- Vertical air motions shift the Doppler spectrum in such a way that $v_D = v_{\text{air}} + v_t$
- 10 – Turbulence and beam-width effects broaden the Doppler spectrum

The shift induced by vertical air motions can be removed if the magnitude of vertical air motion v_{air} is known. In Radenz et al. (2018) a method is presented for measuring v_t and v_{air} with a combination of CR and RWP. The method of Radenz et al. (2018) combines Doppler spectra observed by both instruments in order to remove influence of Rayleigh scattering on the otherwise Bragg-scattering-dominated RWP measurements, resulting in an undisturbed measurement of vertical air motions.

15 The velocity scale of the CR Doppler spectrum is shifted by the measured vertical air motion in order to derive v_t . In the context of this work, v_t is of central importance for the retrieval of particle sizes.

Mie scattering effects are neglected in the context of this work, because we aim on studying small, pristine ice particles. Signal attenuation by these ice particles is also negligible. Turbulence and beam-width broadening are also introducing artifacts. A strongly broadened CR Doppler spectrum might contain unphysical negative terminal fall velocities even after correction

20 of mean vertical air motion. Such effects cannot be removed easily, but luckily they only affect the width and not the mean velocity of the spectrum, which is shown in Section 3.2.

3.2 General principle of the retrieval method

In the present work, a method for deriving N and F of pristine ice particles from combined lidar/CR/RWP measurements is described. An analytical inversion of the measurement values of lidar, CR and RWP is not possible, so numerical inversion

25 techniques have to be applied. For efficient and simple numerical implementation, a lookup table is used which contains the properties of the particle size spectrum and the observable measurement values Z , E , v_t and CR spectral width w . In this section, the mathematical foundations and assumptions for creating this lookup table are explained.

The basic measurement values that are used in the retrieval are the first three moments (Z , v_t and w) derived from the CR Doppler spectra which are corrected for vertical air motion. If no RWP measurements are available, v_t can be replaced by

30 the ratio Z/E with E being the particle extinction coefficient measured by lidar. A retrieval is performed by trying to find a

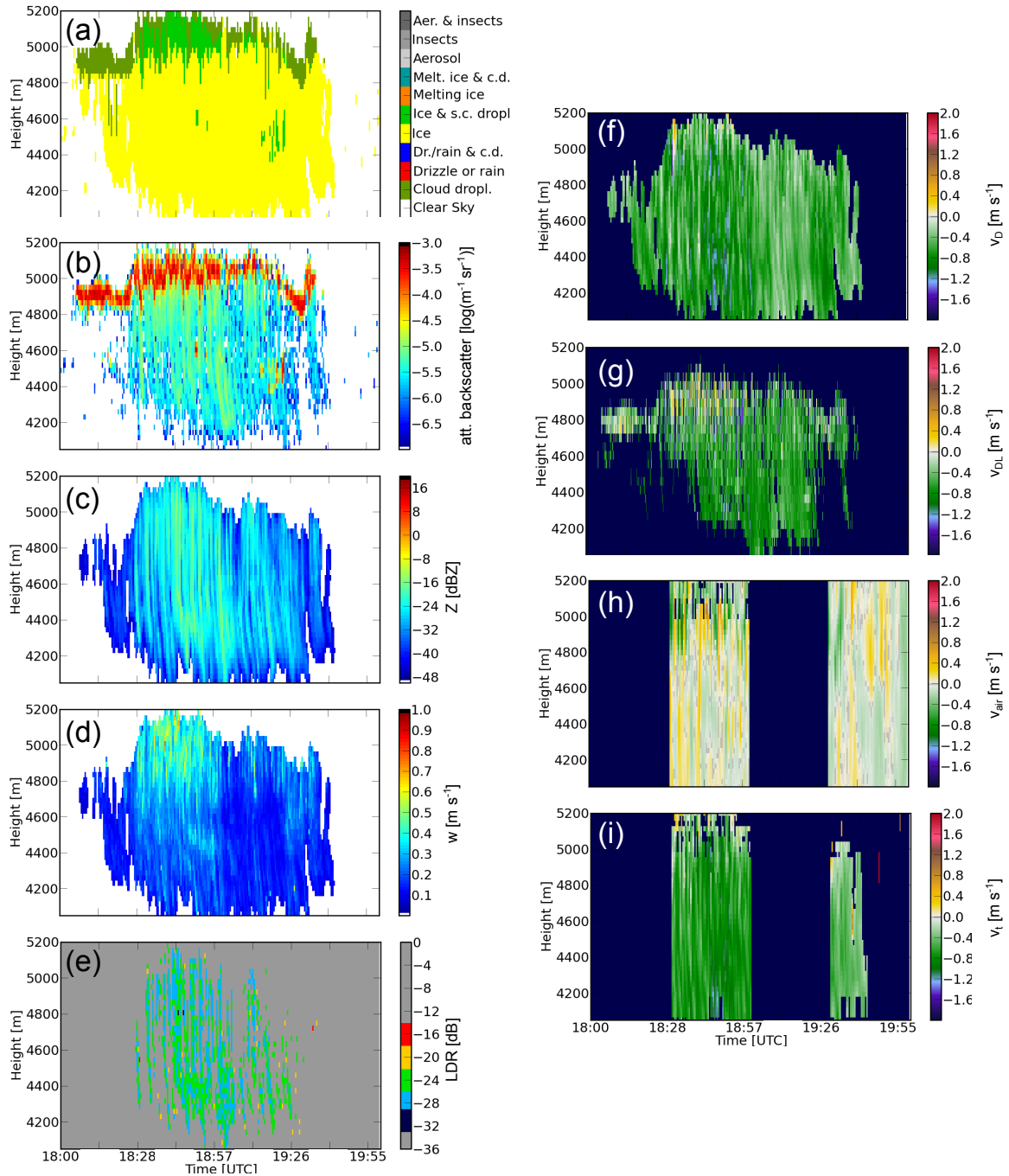


Figure 2. (a) Cloudnet target classification, (b) attenuated backscatter from lidar at 1064nm wavelength, (c) CR reflectivity Z , (d) CR Doppler spectral width w , (e) CR linear depolarization ratio (LDR), (f) CR Doppler velocity v_D , (g) Doppler lidar Doppler velocity v_{DL} , (h) vertical air motions as measured with the RWP v_{air} and (i) reflectivity weighted terminal fall velocity v_t are shown for a mixed-phase cloud layer observed on 11 June 2015 at Lindenberg. v_t and v_{air} are only available in half-hour intervals, because vertical and horizontal wind measurement modes of the RWP are alternating each 30 min.



particle distribution that leads to the same variables as the measured ones. Figure 3 gives an example of this forward modeling approach. Two particle size distributions, characterized by different particle shapes of side planes and column-like particles, respectively, are defined in such a way that the simulated CR Doppler spectrum matches with the one measured. It is visible from this figure that different particle species can lead to very similar cloud radar spectra from significantly different particle size distributions. This is the case because the relationship between mass and terminal fall velocity are different for both particle populations “side planes” and “column-like“. For retrieving N and F , the simulation procedure is done first with a large variety of size distributions which are later compared to the measured values. A schematic overview of the retrieval method used here is given in Fig. 4.

Environmental factors affecting the shape of the CR Doppler spectra are taken into account during the computation of the lookup table. The signal strength of the CR is, e.g., affected by attenuation from water vapor and liquid water particles, air motion shifts the CR Doppler spectrum and turbulence broadens it. In the context of this work, water vapor attenuation is corrected with the method of Cloudnet (Illingworth et al., 2007). Particle attenuation is neglected since we concentrate on cloud layers, in which ice, liquid water and water vapor do not contribute significantly to cloud radar attenuation.

The modified gamma distribution from Delanoë et al. (2005) is assumed here, so we set for the PSD

$$N(D) = N_{\text{total}} C \left(\frac{D}{D_m} \right)^\mu \exp\left(-\left(4 + \mu\right) \frac{D}{D_m}\right) \quad (1)$$

with size parameter D_m (median particle maximum diameter), shape parameter μ (describing the tilt of the distribution) and normalization factor C and the total ice number concentration N_{total} . Particle size spectra are simulated for all particle types mentioned in Table A2 and a variety of realistic combinations of the parameters pressure p , temperature T , CR spectral broadening σ_{total} , size parameter D_m and μ . The ranges and step sizes for all parameters used in this study are found in Table 1.

Table 1. Ranges and step sizes for computation of the lookup table

Parameter	Range low	Range high	Step size	Unit
p	50	1050	50	hPa
T	180	270	10	K
s	0.05	0.5	0.1	ms^{-1}
D_m	$1 \cdot 10^{-5}$	$5 \cdot 10^{-3}$	$25 \cdot 10^{-6}$	m
μ	1	61	1	-

The extensive properties N and F and the measurement quantities Z and E are not used as an input parameter in the forward modeling, because they all linearly depend on N . For the retrieval, only the shape (D_m and μ) of the distribution is of interest. Hence, a normalized version of the PSD with

$$\int N(D) dD = 1 \quad (2)$$

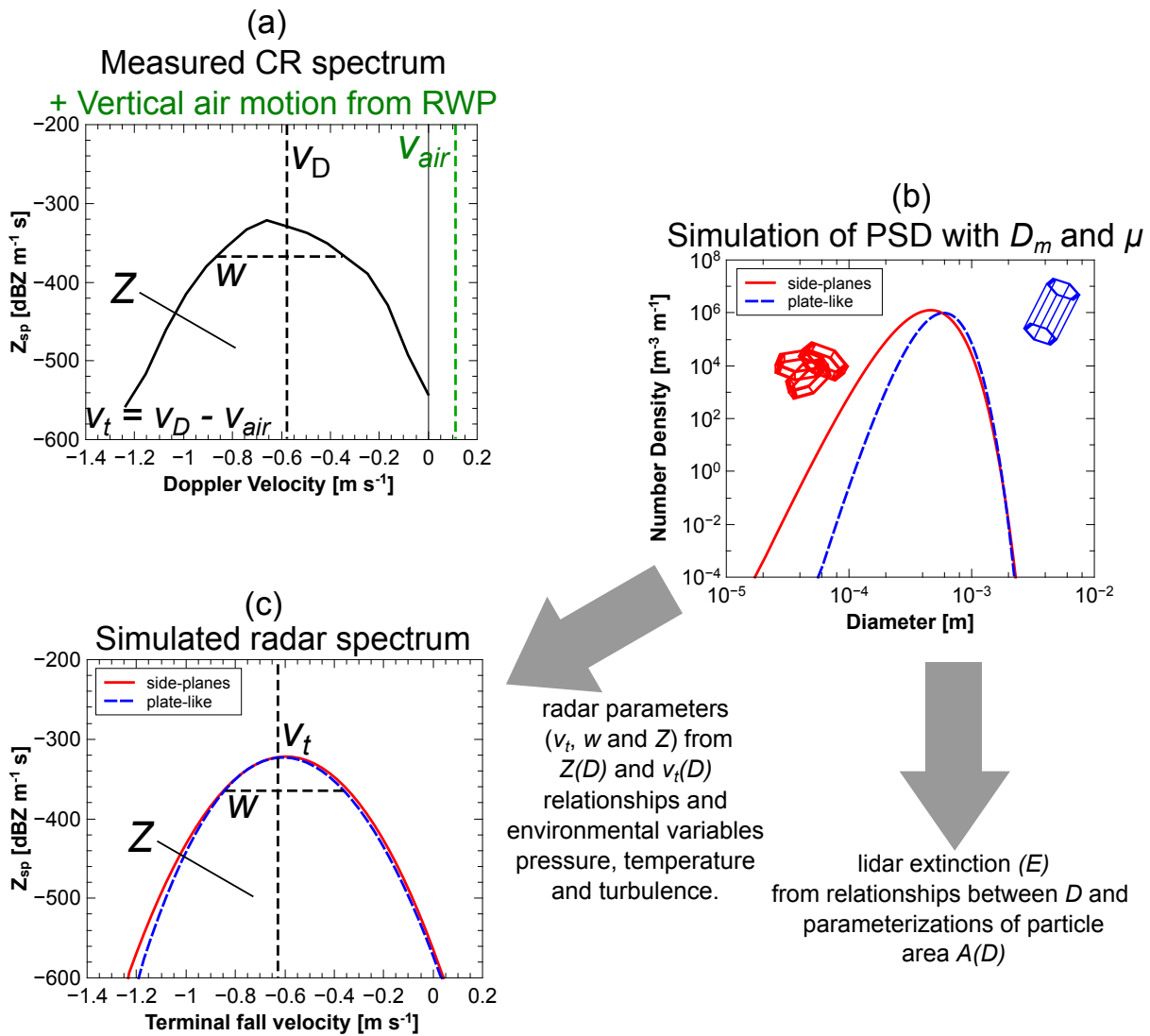


Figure 3. Illustration of the general idea of the retrieval. (a) Example CR Doppler spectrum measured at 4500m height with the CR at Lindenberg on 11 June 2015 at 19:00 UTC (see Fig. 2) with spectral radar reflectivity ($Z_{sp}(v) = Z(v)/\Delta v$ with Doppler spectrum grid length $\Delta v = 0.08 \text{ m s}^{-1}$) first three moments $Z = \int Z(v)dv$, v_t and w . (b) Particle size distribution functions for two different particle populations. (c) Simulated Z_{sp} from both particle size distributions with the same moments as the measured variables.

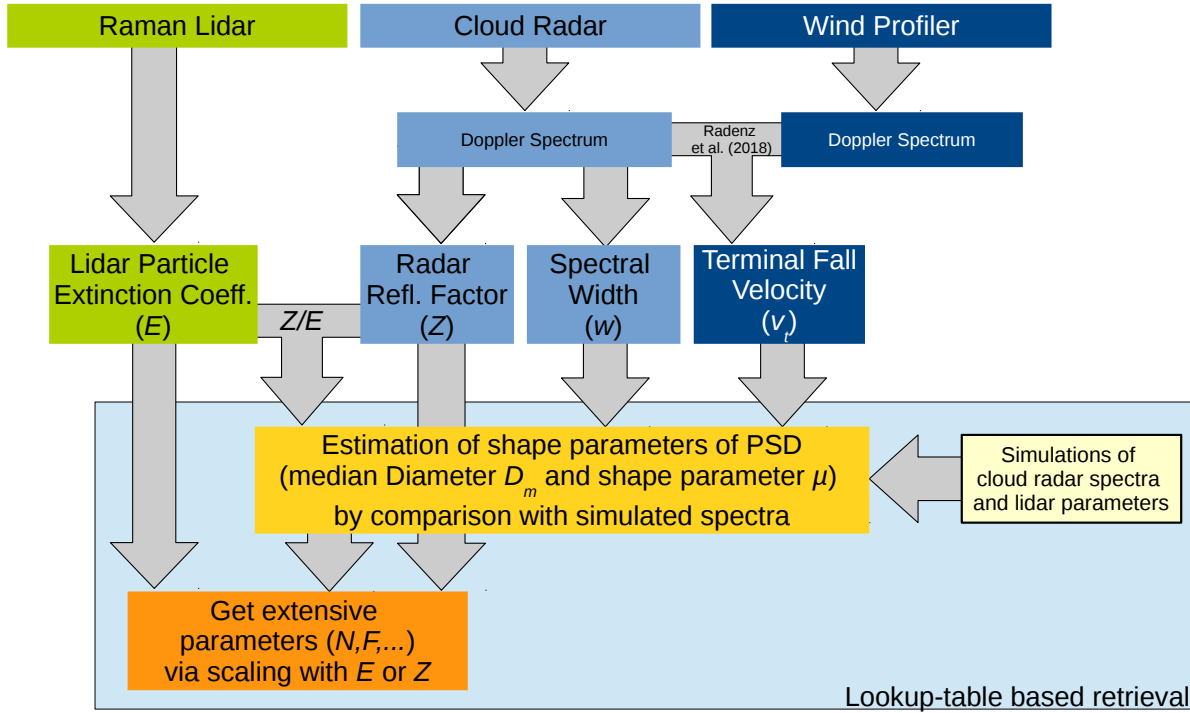


Figure 4. Flowchart of the retrieval algorithm, illustrating the synthesis of data from the remote-sensing instruments with the simulated parameters.

is used. In consequence, all following extensive quantities are derived for a particle number concentration of one particle per cubic meter, indicated by a subscript "1".

A CR Doppler spectrum of Z

$$Z(D) = (K/0.93(6/(\pi 917.0))^2 N(D) m^2(D))/0.001^6 \quad (3)$$

5 is simulated with $K = 0.174$ (dielectric constant for ice at 35 GHz) for ice particles, particle mass $m(D)$ is obtained via Eq. B1. Only small pristine particles are considered in the context of this work and all calculations are done for a CR with 35 GHz operation frequency (8.5 mm wavelength). Since the Mie parameter of these particles is usually smaller than 1, only Rayleigh scattering is considered in this context.

Accordingly, the extensive variables normalized to one particle per cubic meter are normalized number flux

$$10 \quad F_1 = \int N(D) v(D) dD, \quad (4)$$



normalized radar reflectivity factor

$$Z_1 = \int Z(D)dD, \quad (5)$$

and normalized particle extinction coefficient

$$E_1 = 2 \times \int N(D)A(D)dD \quad (6)$$

5 with particle area $A(D)$ obtained from Eq. B2.

From the two latter equations, the reflectivity-to-extinction ratio $Z_1/E_1 = Z/E$ is defined..

For means of completeness, the mean terminal fall velocity measured with a Doppler lidar is given as

$$v_{t,DL} = 2 \times \int N(D)A(D)v(D)dD/E_1. \quad (7)$$

The latter formula assumes that the backscatter from all crystals is only proportional to their projected area. This requires all
 10 crystals to be either randomly oriented or aligned perpendicular to flow direction. Since this would complicate the discus-
 sion of the proof-of-concept approach presented here, we stick to cloud radar measurements of v_t . However, redundancy in
 observations of retrieved parameters increases the robustness of the methodology and quality of the analysis' products.

Simulation of microphysical parameters are only done over the ranges in which the particle properties are valid which are
 given in Table A1. The normalized number concentration

$$15 \quad N_1 = \int N(D)dD \quad (8)$$

is computed in order to ensure that the PSD is well represented within the limits of D . The deviation of N_1 from 1 indicates,
 how many particles are not considered due to the limited range of D . In the context of this work, we discard all calculations in
 which $N_1 < 0.95$, meaning that at maximum 5% of the particles at the upper and/or lower boundary may be not included.

As mentioned before, ice particle size D is the most crucial intensive parameters for the retrieval of N . In the present work we
 20 exploit measurements of v_t in order to come up with an estimation of particle size. Hence, in this section and in Appendix B,
 the relationship between median particle size D_m and v_t is discussed. Mitchell (1996); Heymsfield and Westbrook (2010)
 and Khvorostyanov and Curry (2014) present an analytic theory for calculation of v_t of particles on the basis of four fractal
 parameters, describing mass and area of the particles in dependence of their maximum diameter D (minimum enclosing circle
 for ice crystals, particle diameter for droplets). The resulting formula is

$$25 \quad v(D) = A_v \times D^{B_v} \quad (9)$$

with A_v and B_v also being functions of D dependent on the properties of the air surrounding the falling ice crystal. The
 detailed derivation of the formula is described in Appendix B. Flow-tunnel experiments, e.g., by (Fukuta and Takahashi, 1999)
 have produced the parameterizations of particle shapes needed for derivation of A_v and B_v . Tables A1 and A2 summarize these



parameterizations for deriving mass $m(D)$ and area $A(D)$ from maximum particle diameter (D). The detailed derivation of the latter as well as of $v(D)$ which is used in the following is given in Appendix B.

A CR Doppler spectrum is computed on the terminal-velocity grid by computing $v(D)$ and inverting numerically to $D(v)$. The resulting spectrum $Z(v(D))$ is artificially broadened by numerical folding with the normalized Gaussian distribution

$$5 \quad (2\pi\sigma_{\text{total}}^2)^{-1} \times \exp\left(-0.5\frac{v^2}{\sigma_{\text{total}}^2}\right) \quad (10)$$

with standard deviation σ_{total} , which introduces the combined effects of turbulence and beam width broadening. From this broadened spectrum v_t (first moment) and spectral width w (second central moment) are derived.

Such spectra are computed for a variety of input parameters (p, T, ϵ, D_m and μ) and for each combination of input variables, the input and output parameters are collected in three vectors:

- 10 – $\mathbf{i}_L = (p, T, \sigma, D_m, \mu)_L$ holding the input properties that were used in the calculations.
- $\mathbf{p}_L = (v_t, w, Z/E)_L$ holding the intensive properties of the distribution
- $\mathbf{n}_L = (N_1, F_1, A_1)_L$ containing the normalized extensive properties of the distribution

with subscript L to indicate that these vectors are members of the lookup table. This lookup table containing the three vectors \mathbf{i}, \mathbf{p} and \mathbf{n} is computed for a set of input variables of $p, T, \sigma_{\text{total}}, D$ and μ .

15 3.3 Using terminal fall velocity for deriving particle size

The basis for the retrieval of N is an estimation of D_m . In this section, two relationships – $v_t(D)$ and $Z/E(D)$ – are compared for exemplary particle types and varying properties of the underlying particle size distribution. v_t and Z/E can both be used to derive D_m , because both are steady and differentiable with D_m . It can be seen from Figure 5 that v_t and Z/E show a very similar dependence on D , which is not surprising since both are proportional to m and reciprocal to A . For the purpose of
 20 deriving the size and shape properties of a particle size spectrum both quantities are interchangeable and a direct measurement of v_t can replace a missing Z/E . More importantly, both v_t and Z/E only depend weakly on shape parameter μ of the particle size distribution and the resulting width w of the CR Doppler spectrum.

3.4 Retrieving a result from the lookup table

For retrieving N , an estimation of the particle size distribution must be acquired first. This is done by comparison of measured
 25 parameters with those stored in the lookup table. An overview about the retrieval process is given in Fig. 6. Depending on which parameter is available, this procedure can be done with all combinations of available intensive parameters (currently v_t , w and Z/E). Examples are given in Section 4.

a) Retrieval and uncertainties estimation:

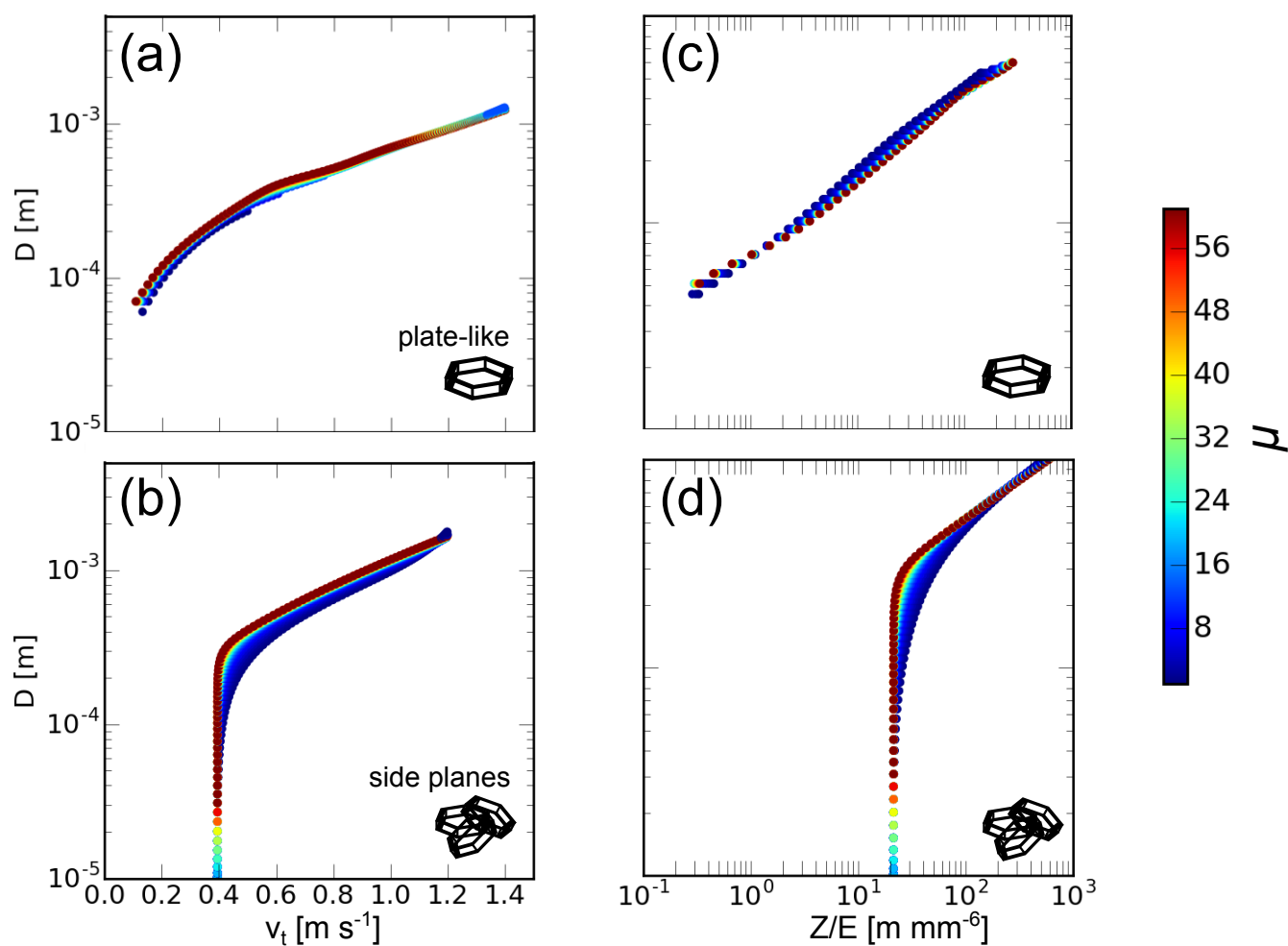


Figure 5. Relationship of v_t with D (a,b) and Z/E with D (c,d) for particles types “plate-like” (a,c) and “side planes” (b,d). v_t graphs are all plotted for $p = 650$ hPa and $T = 255$ K. See Table A2 and Table A1 for the particle properties.

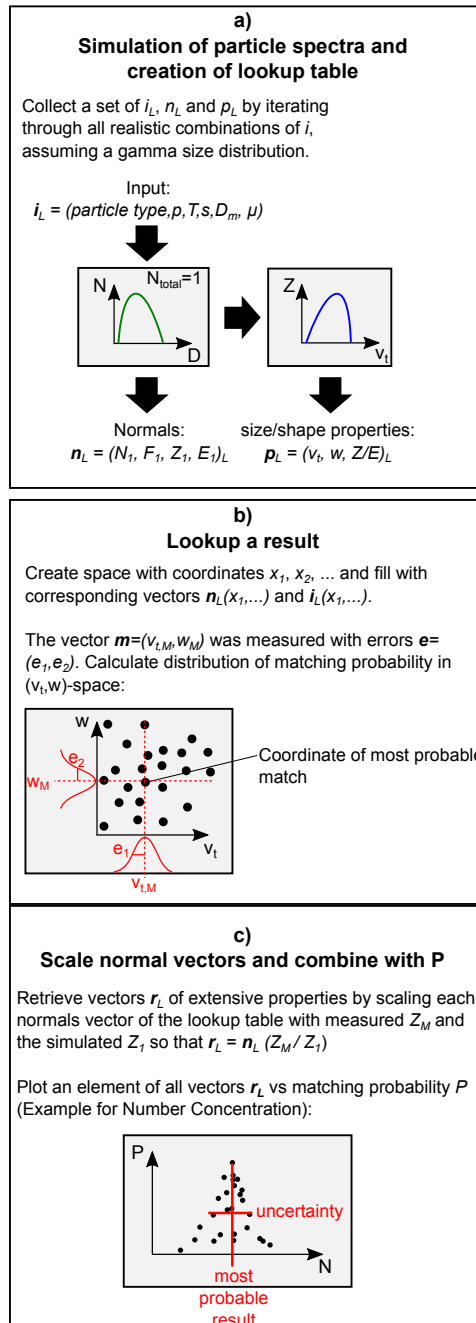


Figure 6. Step-by-step description of the retrieval principle. (a) A lookup table with parameters observable with lidar and radar is created with a set of combinations of particle shape, D_m and μ . (b) The matching probability between the measured parameters and the simulated parameters is searched in the lookup table, resulting in estimations of D_m and μ . (c) The particle size distribution created with the retrieved estimations of D_m and μ is scaled with extensive parameters measured with lidar or CR (E or Z , respectively). The full-width-half-max of the distribution of matching probabilities is considered the uncertainty of the retrieved results. More explanations are given in the text.



A vector with the measured intensive properties \mathbf{m} (possibly p , T , σ , v_t , w and Z/E) is matched with the entries of the lookup table in order to derive D_m and μ of the particle distribution. The matching probability of m to its corresponding values in the lookup table is described by

$$P(\mathbf{p}_L, \mathbf{m}) = \exp\left[-0.5 \sum_i (p_{L,i} - m_i)^2 / e_i^2\right] \quad (11)$$

5 with \mathbf{p}_L being the simulated properties from the lookup table, i index running over the length of \mathbf{p}_L , m containing the corresponding actual measurement values and e the uncertainties assuming a Gaussian error distribution. P is applied to all lines of the lookup table and the matching probability for each single entry is found. As a result a distribution of matching probabilities is derived. At the position of the maximum of all value of P the parameters of the size distribution are retrieved because they represent the best match for the input parameters. The full-width-half-max of P for each derived value is used to
 10 represent the uncertainty of the retrieval. Upper and lower uncertainty may differ, if the distribution of P is not symmetrical around its maximum. A larger uncertainty in one of the measured variables may lead to a broader distribution P for the retrieved variables (see Fig. 6).

b) Scaling:

With the shape of the size distribution known, also the normalized extensive parameters N_1, F_1, Z_1 and E_1 are known. The
 15 desired vector \mathbf{r} of extensive properties (N, F, Z and/or E) is derived by multiplying all of them with the same scaling factor S , which can be either $S_Z = Z/Z_1$ or $S_E = E/E_1$. Scaling adds the measurement uncertainty of Z (CR) or E (lidar).

c) Example:

As an example, a diagram relating F_1 with the intensive properties v_t and w is shown in Fig. 7. The distribution of results in
 (v_t, w) space is shown. From this distribution the most probable solution (here F_1) is selected for measurements of v_t and w .
 20 Multiplication of the selected extensive parameter with the corresponding factor Z/Z_1 yields the scaling factor to derive the actual F and N . The method is here applied in a two dimensional example, but both extensive and intensive parameters can be of arbitrary number.

3.5 Estimation of cross-sensitivity of uncertainties

For estimating the uncertainties introduced by a measurement value on the retrieved quantities, the retrieval is performed for a
 25 fixed set of input parameters and afterwards each single parameter is being varied by one standard deviation. The errors are an estimation of maximum measurement accuracy that can be achieved currently. Table 2 gives a comparison of the errors derived for v_t and Z/E .

The errors of the parameters p , T and s were chosen quite large and, anyway, do not seem to introduce significant errors. It can be seen from this table that for a relatively low v_t of 0.3 m s^{-1} an error of 0.1 m s^{-1} in v_t results in a factor of 3.0 uncertainty
 30 for Z_1 and 0.5 for E_1 . These results are significantly different for a larger v_t of 0.9 m s^{-1} which produces uncertainties of 0.5 and 0.2 for Z_1 and E_1 , respectively. The relatively large uncertainty of 70% in Z/E yields comparable lower uncertainty factors (0.4 for Z_1 and 0.2 for E_1).

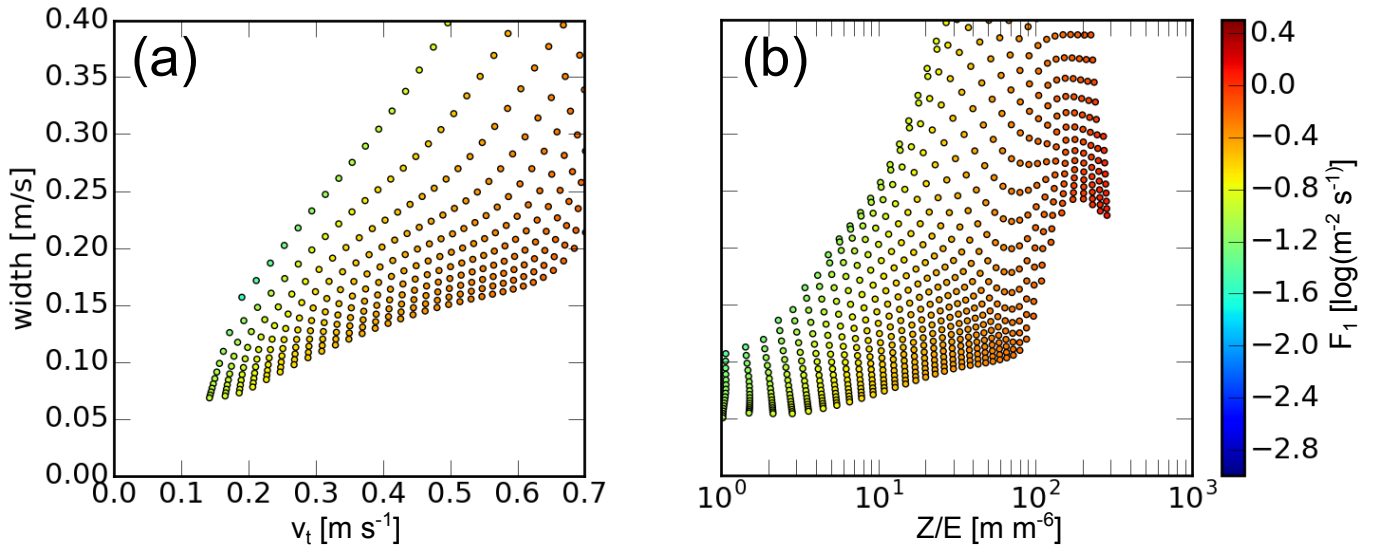


Figure 7. Example of a retrieval of F_1 based on $\mathbf{m} = (v_t, w)$ (a) and $\mathbf{m} = (Z/E, w)$ (b) for the combined particle type “plate-like”.

In this analysis, only methodological errors and random measurement errors have been assumed. Lidar and radar calibration errors are intentionally left out and would add linearly to the discussed uncertainties. However, discussion and treatment of these errors is out of the scope of this work.

Table 2. Ratios between the results of the original and the disturbed retrieval. Row “mean” gives the original input parameters and “error” one the standard deviation uncertainty that has been used for variation.

	mean	error	D_m	μ	F_1	Z_1	E_1
p [pa]	5,8E+4	5,0E+3	0,00	0,00	-0,02	0,00	0,00
T [K]	248,15	10,00	0,00	0,00	-0,04	-0,01	-0,03
s [m s ⁻¹]	0,05	0,20	0,00	0,97	0,07	0,12	0,04
v_t [m s ⁻¹]	0,30	0,10	0,35	0,61	0,40	3,08	0,50
	0,90	0,10	0,10	0,20	0,10	0,50	0,20
Z/E [m mm ⁻⁶]	7,5	5	-0,11	-0,25	-0,20	-0,42	-0,18
	75	50	-0,16	-0,30	-0,17	-0,38	-0,18
width [m s ⁻¹]	0,15	0,05	0,00	-0,46	-0,13	-0,17	-0,12

0.00-0.10
 0.10-0.30
 0.30-1.00
 1.00 - ...

Uncertainty
 Factor

4 Results - Case Study

- Figure 2 shows an altocumulus cloud observed during the COLRAWI-2 campaign at Lindenberg on 11 June 2015. The observed CTT is -10°C . The measured CR LDR let us conclude that the ice particles present are most probably isometric ice crystals (Myagkov et al., 2016). Accordingly, the particle types “plate-like” and “side planes” are chosen for retrieving the microphysical parameters.



The retrieval is done with two forms of the measurement vector which is used for the retrieval. In the first mode Z is the scaling variable and $\mathbf{m} = (v_t, w)$ with a fixed error vector $\mathbf{e} = (0.1 \text{ ms}^{-1}, 0.1 \text{ ms}^{-1})$. In this mode, only RWP and CR are used. v_t derived with the method of Radenz et al. (2018), attenuation corrected CR measurements of Z and w are also used for the retrieval. p and T are acquired from the European Center for Medium-Range Weather Forecast Integrated Forecast (ECMWF IFS) dataset. Figure 8 shows the result of the lookup-table-based retrieval with the measurement vector $\mathbf{m} = (v_t, w)$ and Z as scaling variable. The retrieval shows plausible results for D , μ , N and F with about an order of magnitude uncertainty which is relatively constant all over the case (see Fig. 9). The large uncertainty results from a very broad probability distribution, due to a fast change in the lower part of $v_t(D_m)$ for this particle type (see Fig. 5). In the second mode all parameters are the same, except that $\mathbf{m} = (Z/E, w)$ and $\mathbf{e} = ((\Delta Z + \Delta E) \cdot Z/E, 0.1 \text{ ms}^{-1})$ with relative errors $\Delta Z = 0.2$ and $\Delta E = 0.1$. Extinction is derived by multiplication of the lidar backscatter β with a lidar ratio of 32 Sr^{-1} which is typical for ice crystals (Haarig et al., 2016), using the Klett-Fernald approach (Seifert et al., 2007). In the latter case, only lidar and cloud radar are used for retrieval.

In both modes, uncertainties are derived from the distribution of P just as indicated in Fig. 6. As a means of quality control, values are only taken into account if $P > 0.9$ meaning that the retrieval is within the limits and a realistic results is found. For the particle type “plate-like” the results of the retrieval vary within a factor of 3 between both modes. For the particle type “side planes” the results differ by less than ten percent. Uncertainties of N and F are about a factor of 6 for the retrieval with v_t and about 3 for retrieval with Z/E , respectively. Averaged results for N and F for all four combinations of particle types and retrieval methods are given in Table 3.

Table 3. Retrieval results for the case study at 4500m height for different retrieval modes and particle types.

Particle Type	measurement vector \mathbf{m}	Mean N [m^{-3}]	Mean F [$\text{m}^{-2} \text{ s}^{-1}$]	mean uncertainty factor
plate-like	(v_t, w)	6226	1377	+4/-4
plate-like	$(Z/E, w)$	2025	502	+2/-1.5
side planes	(v_t, w)	969	481	+5/-5
side planes	$(Z/E, w)$	924	450	+3/-2

5 Conclusions and Discussion

A method has been demonstrated to retrieve the size and shape parameters of particle size distributions from remote-sensing measurements of either E , Z and w or v_t and w which can be used to calculate N and F . Both combinations of input parameter have been tested against each other and are found to produce results within the same order of magnitude. Uncertainties of the retrieval based on v_t are found to be larger than for the estimation based on Z/E . Larger retrieval uncertainties occur at smaller v_t for which the change of D with v_t is especially strong.

The paper presents a first step towards the usage of the unique direct measurements of v_t of small ice particles for retrieval of their size, shape and number concentration. The forward modeling method used here for derivation of the observable measurement parameters is simple, but any other methods for CR forward modeling (Kollias et al., 2011) may be applicable for

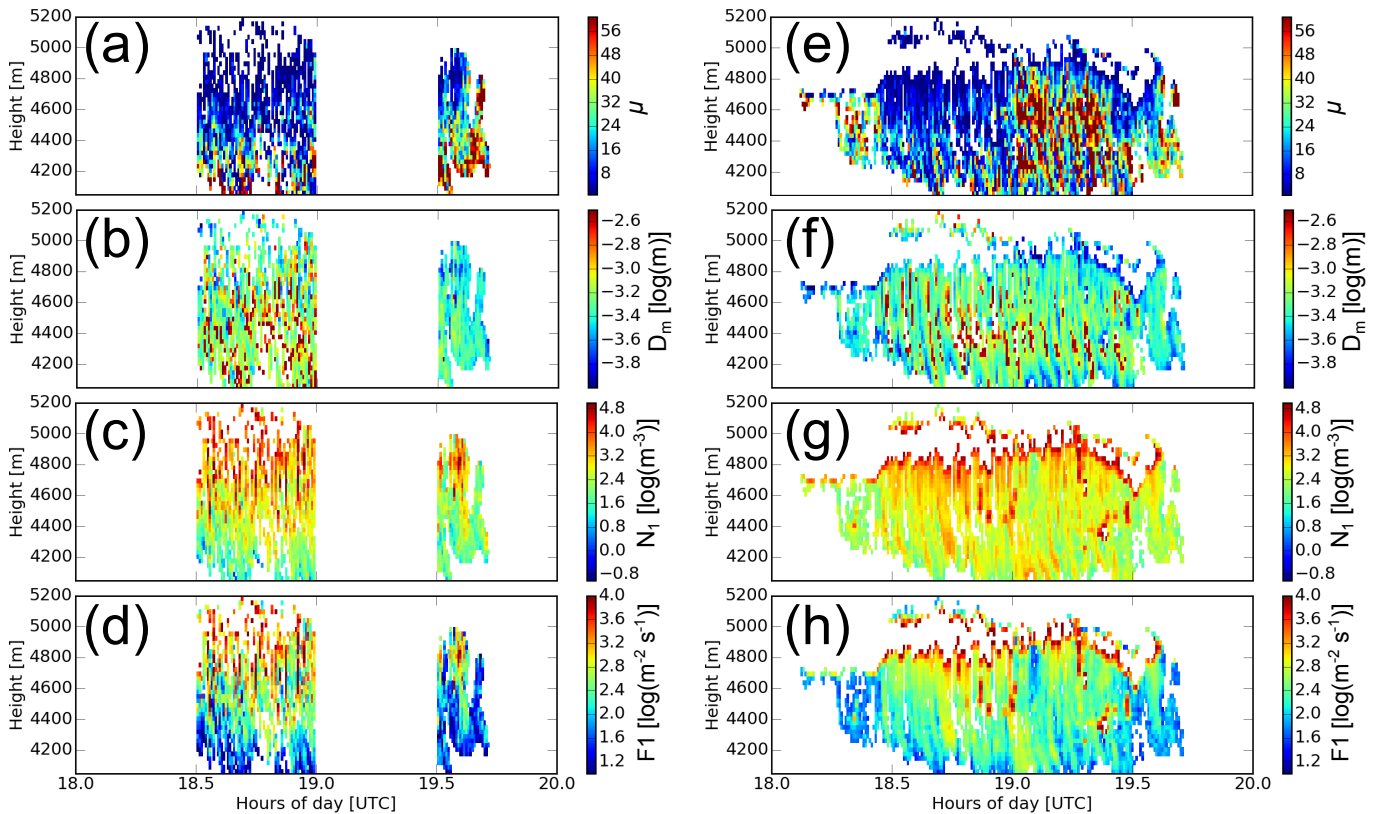


Figure 8. Results of retrieval based on v_t (left column) and Z/E (right column) for the particle type “plate-like”. Combined CR / RWP measurements are only available in the second half of each hour. Different retrieved parameters are shown: (a,e) spectral width parameter μ , (b,f) median Diameter D_m , (c,g) number concentration N and (d,h) particle number flux F .

computation of the lookup table. The present work also shows that it might be beneficial to use v_t derived from combined CR/RWP measurements in other forward iterating models like the one of Ceccaldi et al. (2013).

The presented method is essentially applicable to all remote-sensing facilities that provide lidar particle extinction coefficient and CR (e.g. from the European Aerosols Clouds and Trace gases Infrastructure or the US program for Atmospheric Radiation
 5 Monitoring). Combinations of lidar and radar prove most robust in terms of retrieval uncertainties. However, an error of less than 0.1 ms^{-1} also allows keeping methodological uncertainties for a retrieval of N and F in the range between a factor of 0.5 and 3, which brings the method to the edge of applicability. The method is crucial for investigation of nucleation and growth of small ice particles in optically thick clouds for which no other method can provide accurate estimations of N and F .

The forward model used here is transparent and instructive, but other forward iteration methods might be used in future as
 10 well. In the context of this work, the lookup table approach is used primarily for an analysis of retrieval uncertainties due to input measurement errors. Typing of the pristine particles on the basis of radar depolarization measurements is crucial for the methodology presented here. It is currently a field of intensive research (Bühl et al., 2016; Myagkov et al., 2016) and is, hence,

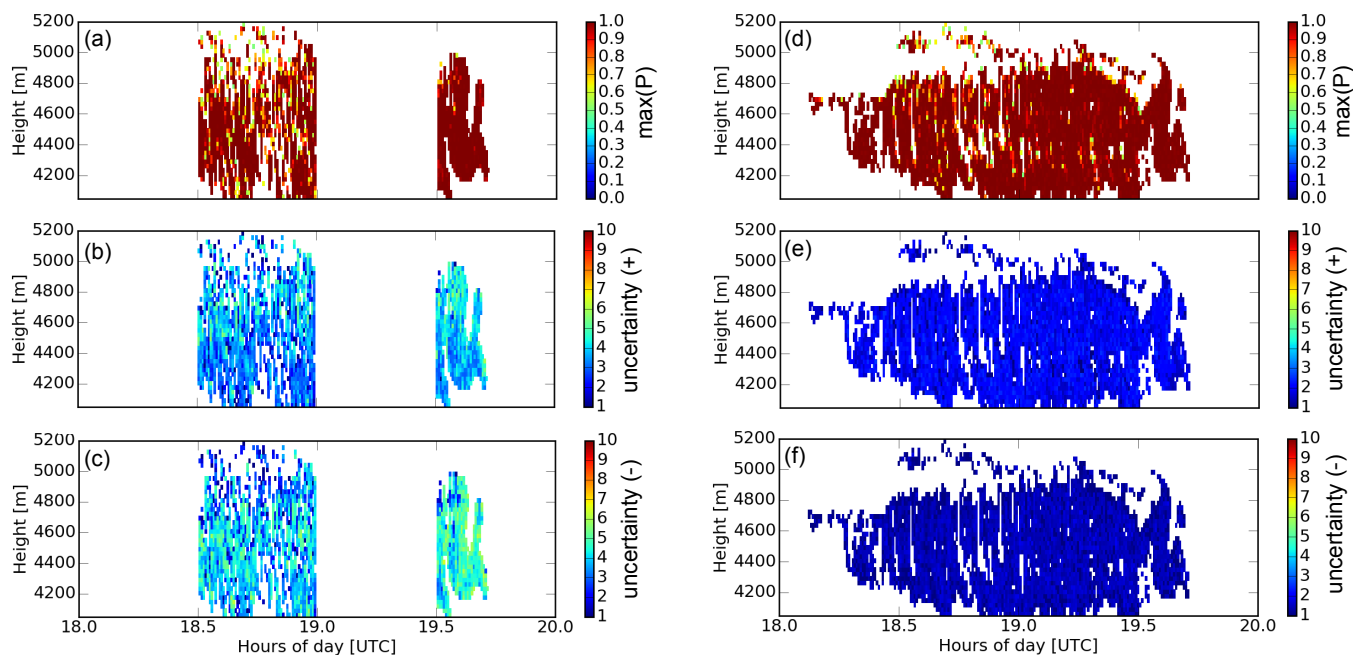


Figure 9. Maximum probability of P for each retrieval (a,d) are shown together with upper (b,e) and lower (c,f) uncertainties for retrieved parameters of Fig. 8.

left out of this work. The same applies to the accurate calibration of the CR which is a necessary prerequisite for the technique presented here (Ewald et al., 2017), but also not covered in the present work.

Several issues need a solution for successful application of the method in future:

- Particle typing has to be improved. Recently developed methods, employing scanning techniques (Myagkov et al., 2016) are more sophisticated and especially show better performance under low signal conditions. Those techniques were not yet available during the COLRAWI-2 campaign, but pose great opportunities for future application in the context of the present work.
- Uncertainties in CR calibration have not been taken into account here, because those errors are essentially unknown. However, great effort is going on to come up with a solution for this problem.
- Matching between the CR and lidar beam has to be improved in order to avoid artifacts under complex situations.
- Direct information about local turbulence have to be taken into account to avoid errors in the estimation of the shape parameter μ .

Given the downside of less flexibility, there are distinct advantages of the lookup table approach over classic forward iteration methods. E.g., all possible results within the uncertainty range of the input variables are found at once. There is no risk that

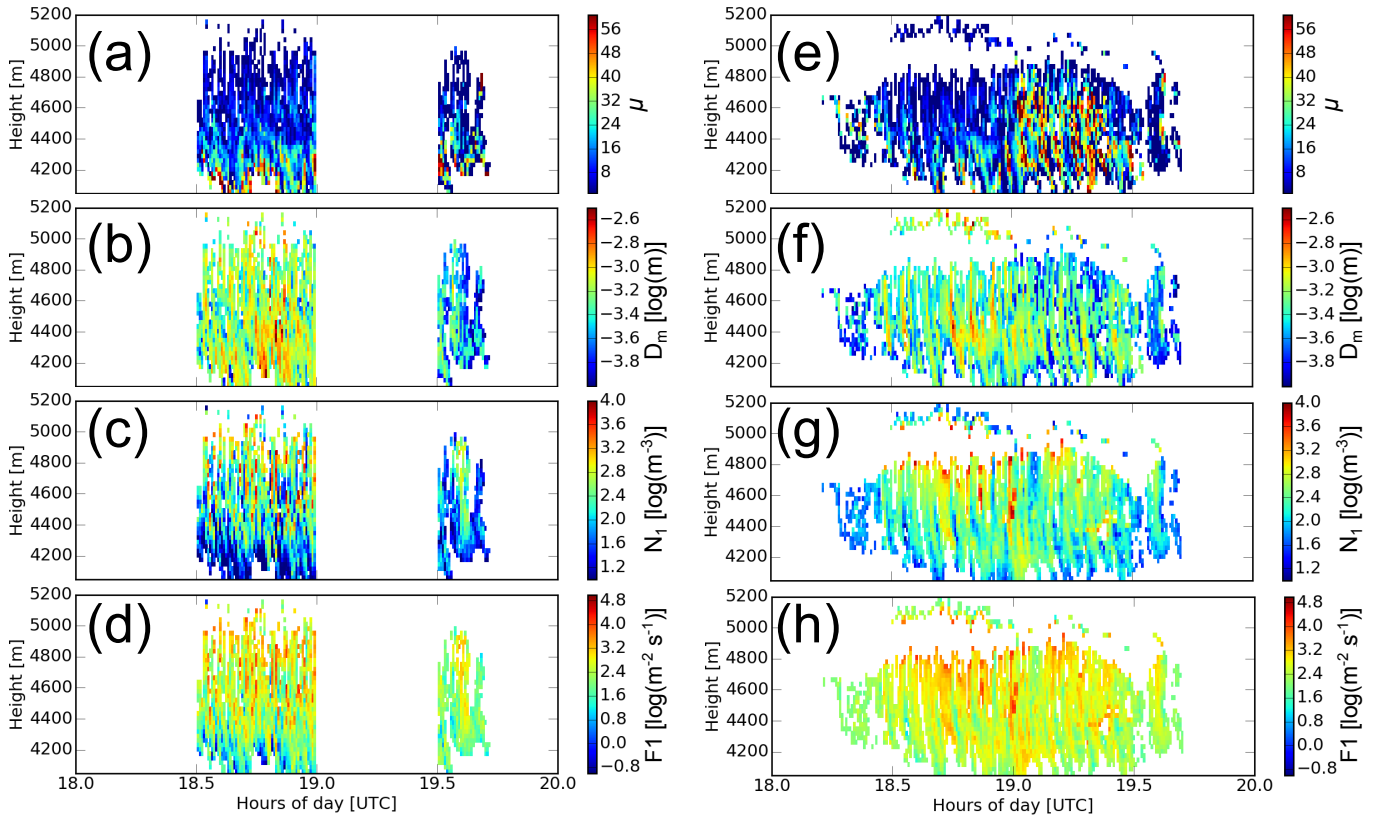


Figure 10. Same as Fig. 8 but for particle type “side planes”.

the method “gets stuck” in a local minimum. A lookup table approach also has the distinct advantage that numerical forward modeling and the actual retrieval are fully separable. Challenges of the approach are extensive memory needs and more effort in evaluation of the results. The method is transparent and it can be implemented easily in a numerically very efficient way. The computation of a case study as shown, e.g., in Fig. 8 takes less than a second on a state of the art desktop computer including

5 estimation of retrieval uncertainties.

Appendix A: Mass and area power law relationships

Table A1 gives parameterizations of m and A for different particle types according to Mitchell (1996). All values are given in cgs notation. Conversion to SI system is done with the formula

$$\alpha_{SI} = \alpha_{CGS} * 100^{\beta_{CGS}} / 1000 \quad (A1)$$

$$10 \quad \gamma_{SI} = \alpha_{CGS} * 100^{\sigma_{CGS}} / 10000. \quad (A2)$$

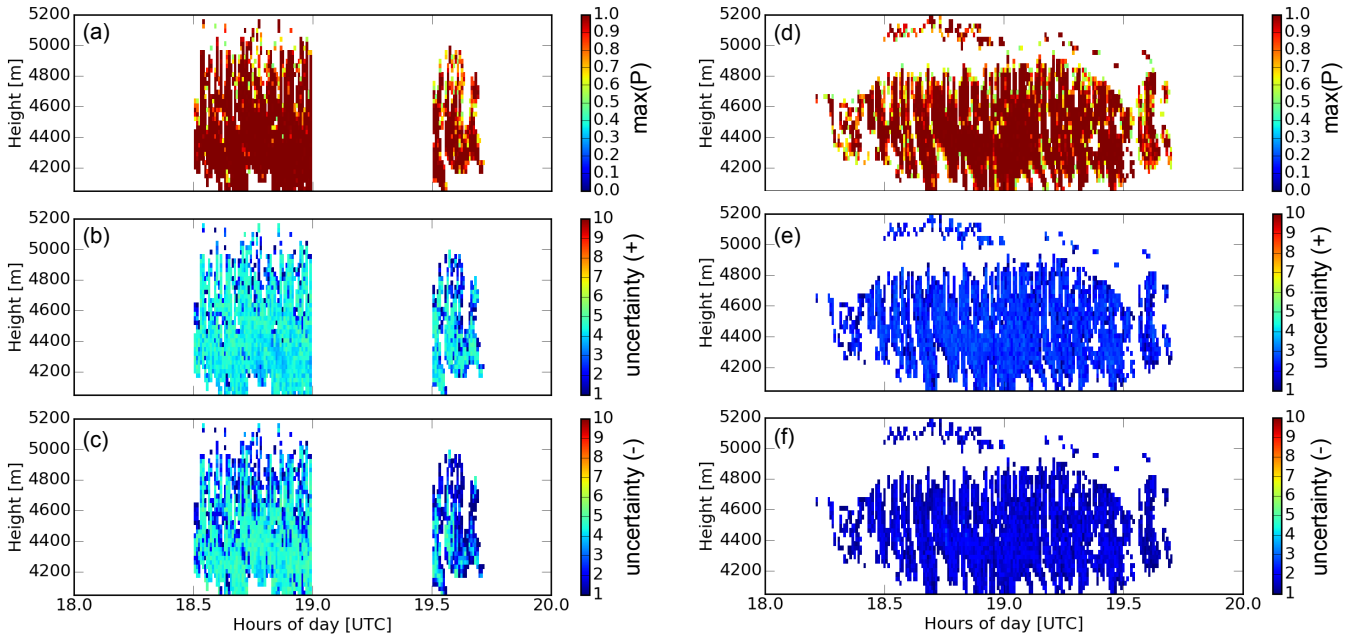


Figure 11. Maximum probability of P for each retrieval (a,d) are shown together with upper (b,e) and lower (c,f) uncertainties for retrieved parameters of Fig. 10.

The lookup table used in this paper is computed for all particle types with a single parameterization from Table A1. Additional particle species are defined in Table A2 that include a transition to aggregate particle types at the upper limit of D .

Appendix B: Calculation of terminal fall velocity

An estimation of v_t is derived from parameterized particle mass m and area A .

$$5 \quad m(D) = \alpha D^\beta \quad (\text{B1})$$

$$A(D) = \gamma D^\sigma \quad (\text{B2})$$

$$g = 9.81 \text{ms}^{-2},$$

The density of the air

$$\rho_{\text{air}} = p / (R_{\text{air}} T) \quad (\text{B3})$$

10 with $R_{\text{air}} = 287.058 \text{ J kg}^{-1} \text{ K}^{-1}$ and kinematic viscosity

$$\nu = \eta_{\text{air}} / \rho_{\text{air}} \quad (\text{B4})$$



Table A1. Values for α , β , γ and σ as well as their valid ranges (D_{\min} ... D_{\max}) used in the context of this work.

Particle Type	D_{\min}	D_{\max}	α_{CGS}	β_{CGS}	γ_{CGS}	σ_{CGS}
Hexagonal Plates	0	99	0.0065	2.45	0.24	1.85
	99	400	0.00739	2.45	0.65	2
Hexagonal Columns	0	99	0.1677	2.91	0.684	2
	99	300	0.00166	1.91	0.0696	1.5
	300	600	0.000907	1.74	0.0512	1.414
Rimed Long Columns	600	2000	0.00145	1.8	0.0512	1.414
Sector Branched Crystal	0	40	0.00614	2.42	0.24	1.85
	40	8000	0.00142	2.02	0.55	1.97
Broad Branched Crystal	0	100	0.00583	2.42	0.24	1.85
	100	1000	0.000516	1.8	0.21	1.76
Stellar Crystal Broad Arms	0	90	0.00583	2.42	0.24	1.85
	0	1500	0.00027	1.67	0.11	1.63
Densely rimed dendrides	0	4000	0.015	2.3	0.21	1.76
Side planes	0	2500	0.00419	2.3	0.2285	1.88
Bullet Rosettes	0	1000	0.00308	2.26	0.0869	1.57
Aggregates side planes	0	1000000	0.0033	2.2	0.02285	1.88
Aggregates thin planes	600	1000000	0.00145	1.8	0.2285	1.88
Aggregates mixture	0	8000	0.0028	2.1	0.2285	1.88
Assemblage planar polycrystals	0	1000000	0.00739	2.45	0.2285	1.88
Lump graupel	500	3000	0.049	2.8	0.5	2
Hail	5000	25000	0.466	3	0.625	2

Table A2. Combined particles types used in the context of this work

Combined type No.	Combined type Name	Parameterizations	Ranges
1	plate-like	Hexagonal Columns	0...600 μm
		Aggregates thin plates	600...2500 μm
2	column-like	Hexagonal Plates	0...400 μm
		Rimed long columns	600...2000 μm



with $\eta_{\text{air}} = 1.59e - 5 + (1.725e - 5 - 1.59e - 5) * (T - 250.0) / 25.0 \text{ kg m}^{-1} \text{ s}^{-1}$ are used to derive the “Best-Number”

$$X(D) = 2m_D(1 - \rho_{\text{air}}/\rho_p)gD^2/(A_D\rho_p\nu^2). \quad (\text{B5})$$

The two constants

$$b_{\text{Re}} = C_1 X^{0.5} / (2((1 + C_1 X^{0.5})^{0.5} - 1)(1 + C_1 X^{0.5})^{0.5}) \quad (\text{B6})$$

$$5 \quad a_{\text{Re}} = \delta_0^2 / 4.0((1 + C_1 X^{0.5})^{0.5} - 1)^2 / X^{b_{\text{Re}}} \quad (\text{B7})$$

with $C_1 = 4/(\delta_0^2 C_0^{0.5})$ are defined. The different constants that apply for different particle types are defined in Table B1. The Reynolds number

$$Re(D) = a_{\text{Re}} e(D) X(D)^{b_{\text{Re}}(D)} \quad (\text{B8})$$

is derived and two additional functions are defined:

$$10 \quad A_v = a_{\text{Re}} \nu^{1-2b_{\text{Re}}} (2\alpha g / (\rho_{\text{air}} \gamma))^{b_{\text{Re}}} \quad (\text{B9})$$

$$B_v = b_{\text{Re}} * (\beta - \sigma + 2) - 1 \quad (\text{B10})$$

With these results, v_t can be expressed as a closed function of D .

$$v(D) = A_v(D) \times D^{B_v(D)} \quad (\text{B11})$$

Table B1. Parameters for velocity calculations (Boehm 1989,1992):

Particle Type	C_0	δ_0	ρ_p [kg m ⁻³]
Ice crystals	0.6	5.83	934.0
Hail/graupel	0.292	9.06	934.0
Rain/Drizzle droplets	0.292	9.06	1000.0

B1

- 15 *Author contributions.* Johannes Buehl initiated the COLRAWI measurements, conceived the retrieval method and wrote the paper. Patric Seifert and Martin Radenz contributed methods for data evaluation and interpretation. Holger Baars evaluated the Raman-lidar data. Albert Ansmann supervised the work and supported the manuscript preparation.



Competing interests. The authors declare no competing interests.

Acknowledgements. The research leading to these results has received funding from the European Union's Horizon 2020 research and innovation programme under grant agreement no. 654109 (ACTRIS-2) and previously from the European Union Seventh Framework Programme (FP7/2007–2013) under grant agreement no. 262254 (ACTRIS) and no. 603445 (BACCHUS) as well as from the Cloudnet project (European Union contract EVK2-2000-00611). We thank Volker Lehmann, Ulrich Gørsdorf and Ronny Leinweber of MOL/RAO Lindenberg for the lively cooperation and for performing the measurements with RWP, CR and DL. The PollyXT used in this study is under the supervision of Ina Mattis (DWD).



References

- Baars, H., Seifert, P., Engelmann, R., and Wandinger, U.: Target categorization of aerosol and clouds by continuous multiwavelength-polarization lidar measurements, *Atmospheric Measurement Techniques*, 10, 3175–3201, <https://doi.org/10.5194/amt-10-3175-2017>, <https://www.atmos-meas-tech.net/10/3175/2017/>, 2017.
- 5 Battaglia, A., Westbrook, C. D., Kneifel, S., Kollias, P., Humpage, N., Löhnert, U., Tyynelä, J., and Petty, G. W.: G band atmospheric radars: new frontiers in cloud physics, *Atmospheric Measurement Techniques*, 7, 1527–1546, <https://doi.org/10.5194/amt-7-1527-2014>, <https://www.atmos-meas-tech.net/7/1527/2014/>, 2014.
- Bühl, J., Leinweber, R., Görndorf, U., Radenz, M., Ansmann, A., and Lehmann, V.: Combined vertical-velocity observations with Doppler lidar, cloud radar and wind profiler, *Atmospheric Measurement Techniques*, 8, 3527–3536, <https://doi.org/10.5194/amt-8-3527-2015>,
10 <http://www.atmos-meas-tech.net/8/3527/2015/>, 2015.
- Bühl, J., Seifert, P., Myagkov, A., and Ansmann, A.: Measuring ice- and liquid-water properties in mixed-phase cloud layers at the Leipzig Cloudnet station, *Atmospheric Chemistry and Physics*, 16, 10609–10620, <https://doi.org/10.5194/acp-16-10609-2016>, <http://www.atmos-chem-phys.net/16/10609/2016/>, 2016.
- Ceccaldi, M., Delanoë, J., Hogan, R. J., Pounder, N. L., Protat, A., and Pelon, J.: From CloudSat-CALIPSO to EarthCare: Evolution of the
15 DARDAR cloud classification and its comparison to airborne radar-lidar observations, *Journal of Geophysical Research: Atmospheres*, 118, 7962–7981, <https://doi.org/10.1002/jgrd.50579>, <https://agupubs.onlinelibrary.wiley.com/doi/abs/10.1002/jgrd.50579>, 2013.
- Delanoë, J., Protat, A., Testud, J., Bouniol, D., Heymsfield, A. J., Bansemmer, A., Brown, P. R. A., and Forbes, R. M.: Statistical properties of the normalized ice particle size distribution, *Journal of Geophysical Research: Atmospheres*, 110, <https://doi.org/10.1029/2004JD005405>, <https://agupubs.onlinelibrary.wiley.com/doi/abs/10.1029/2004JD005405>, 2005.
- 20 Eidhammer, T., DeMott, P. J., Prenni, A. J., Petters, M. D., Twohy, C. H., Rogers, D. C., Stith, J., Heymsfield, A., Wang, Z., Pratt, K. A., Prather, K. A., Murphy, S. M., Seinfeld, J. H., Subramanian, R., and Kreidenweis, S. M.: Ice Initiation by Aerosol Particles: Measured and Predicted Ice Nuclei Concentrations versus Measured Ice Crystal Concentrations in an Orographic Wave Cloud, *Journal of the Atmospheric Sciences*, 67, 2417–2436, <https://doi.org/10.1175/2010JAS3266.1>, 2010.
- Engelmann, R., Kanitz, T., Baars, H., Heese, B., Althausen, D., Skupin, A., Wandinger, U., Komppula, M., Stachlewska, I. S., Amiridis,
25 V., Marinou, E., Mattis, I., Linné, H., and Ansmann, A.: The automated multiwavelength Raman polarization and water-vapor lidar Polly^{XT}: the neXT generation, *Atmospheric Measurement Techniques*, 9, 1767–1784, <https://doi.org/10.5194/amt-9-1767-2016>, <https://www.atmos-meas-tech.net/9/1767/2016/>, 2016.
- Ewald, F., Gross, S., Hagen, M., Hirsch, L., and Delanoë, J.: Calibration of a 35-GHz Airborne Cloud Radar: Lessons Learned and Inter-
30 comparison with a 94-GHz Airborne Cloud Radar, in: *EGU General Assembly Conference Abstracts*, vol. 19 of *EGU General Assembly Conference Abstracts*, p. 14871, 2017.
- Fukuta, N. and Takahashi, T.: The Growth of Atmospheric Ice Crystals: A Summary of Findings in Vertical Supercooled Cloud Tunnel Studies, *J. Atmos. Sci.*, 56, 1963–1979, [http://dx.doi.org/10.1175/1520-0469\(1999\)056<1963:TGOAIC>2.0.CO;2](http://dx.doi.org/10.1175/1520-0469(1999)056<1963:TGOAIC>2.0.CO;2), 1999.
- Görndorf, U., Lehmann, V., Bauer-Pfundstein, M., Peters, G., Vavriv, D., Vinogradov, V., and Volkov, V.: A 35-GHz Polarimetric Doppler
35 Radar for Long-Term Observations of Cloud Parameters—Description of System and Data Processing, *J. Atmos. Oceanic Technol.*, 32, 675–690, <http://dx.doi.org/10.1175/JTECH-D-14-00066.1>, 2015.



- Haarig, M., Engelmann, R., Ansmann, A., Veselovskii, I., Whiteman, D. N., and Althausen, D.: 1064 nm rotational Raman lidar for particle extinction and lidar-ratio profiling: cirrus case study, *Atmospheric Measurement Techniques*, 9, 4269–4278, <https://doi.org/10.5194/amt-9-4269-2016>, <https://www.atmos-meas-tech.net/9/4269/2016/>, 2016.
- Heymsfield, A. J. and Westbrook, C. D.: Advances in the estimation of ice particle fall speeds using laboratory and field measurements, *Journal of the Atmospheric Sciences*, 67, 2469–2482, <http://dx.doi.org/10.1175/2010JAS3379.1>, 2010.
- Illingworth, A. J., Hogan, R. J., O'Connor, E. J., Bouniol, D., Delanoë, J., Pelon, J., Protat, A., Brooks, M. E., Gaussiat, N., Wilson, D. R., Donovan, D. P., Baltink, H. K., van Zadelhoff, G.-J., Eastment, J. D., Goddard, J. W. F., Wrench, C. L., Haeffelin, M., Krasnov, O. A., Russchenberg, H. W. J., Piriou, J.-M., Vinit, F., Seifert, A., Tompkins, A. M., and Willén, U.: Cloudnet, *Bulletin of the American Meteorological Society*, 88, 883–898, <http://dx.doi.org/10.1175/BAMS-88-6-883>, 2007.
- Khvorostyanov, V. I. and Curry, J. A.: *Thermodynamics, kinetics, and microphysics of clouds*, Cambridge University Press, 2014.
- Kneifel, S., Kulie, M., and Bennartz, R.: A triple-frequency approach to retrieve microphysical snowfall parameters, *Journal of Geophysical Research: Atmospheres*, 116, 2011.
- Kollias, P., Rémillard, J., Luke, E., and Szyrmer, W.: Cloud radar Doppler spectra in drizzling stratiform clouds: 1. Forward modeling and remote sensing applications, *Journal of Geophysical Research: Atmospheres*, 116, <https://doi.org/10.1029/2010JD015237>, <https://agupubs.onlinelibrary.wiley.com/doi/abs/10.1029/2010JD015237>, 2011.
- Korolev, A., McFarquhar, G., Field, P. R., Franklin, C., Lawson, P., Wang, Z., Williams, E., Abel, S. J., Axisa, D., Borrmann, S., Crosier, J., Fugal, J., Krämer, M., Lohmann, U., Schlenczek, O., Schnaiter, M., and Wendisch, M.: Mixed-Phase Clouds: Progress and Challenges, *Meteorological Monographs*, 58, 5.1–5.50, <https://doi.org/10.1175/AMSMONOGRAPHIS-D-17-0001.1>, <https://doi.org/10.1175/AMSMONOGRAPHIS-D-17-0001.1>, 2017.
- Lehmann, V. and Teschke, G.: Wavelet based methods for improved wind profiler signal processing, *Annales Geophysicae*, 19, 825–836, <https://hal.archives-ouvertes.fr/hal-00316878>, 2001.
- Mitchell, D. L.: Use of mass- and area-dimensional power laws for determining precipitation particle terminal velocities, *Journal of the Atmospheric Sciences*, 53, 1710–1723, [http://dx.doi.org/10.1175/1520-0469\(1996\)053<1710:UOMAAD>2.0.CO;2](http://dx.doi.org/10.1175/1520-0469(1996)053<1710:UOMAAD>2.0.CO;2), 1996.
- Mülmenstädt, J., Sourdeval, O., Delanoë, J., and Quaas, J.: Frequency of occurrence of rain from liquid-, mixed-, and ice-phase clouds derived from A-Train satellite retrievals, *Geophysical Research Letters*, 42, 6502–6509, <https://doi.org/10.1002/2015GL064604>, 2015.
- Myagkov, A., Seifert, P., Wandinger, U., Bühl, J., and Engelmann, R.: Relationship between temperature and apparent shape of pristine ice crystals derived from polarimetric cloud radar observations during the ACCEPT campaign, *Atmospheric Measurement Techniques*, 9, 3739–3754, <https://doi.org/10.5194/amt-9-3739-2016>, <http://www.atmos-meas-tech.net/9/3739/2016/>, 2016.
- Päschke, E., Leinweber, R., and Lehmann, V.: An assessment of the performance of a 1.5 μm Doppler lidar for operational vertical wind profiling based on a 1-year trial, *Atmospheric Measurement Techniques*, 8, 2251–2266, <https://doi.org/10.5194/amt-8-2251-2015>, <https://www.atmos-meas-tech.net/8/2251/2015/>, 2015.
- Radenz, M., Bühl, J., Lehmann, V., Görsdorf, U., and Leinweber, R.: Combining cloud radar and radar wind profiler for a value added estimate of vertical air motion and particle terminal velocity within clouds, *Atmospheric Measurement Techniques*, 11, 5925–5940, <https://doi.org/10.5194/amt-11-5925-2018>, <https://www.atmos-meas-tech.net/11/5925/2018/>, 2018.
- Seifert, P., Ansmann, A., Müller, D., Wandinger, U., Althausen, D., Heymsfield, A. J., Massie, S. T., and Schmitt, C.: Cirrus optical properties observed with lidar, radiosonde, and satellite over the tropical Indian Ocean during the aerosol-polluted northeast and clean maritime southwest monsoon, *Journal of Geophysical Research: Atmospheres*, 112, <https://doi.org/10.1029/2006JD008352>, <https://agupubs.onlinelibrary.wiley.com/doi/abs/10.1029/2006JD008352>, 2007.



- Sekelsky, S. M., Ecklund, W. L., Firda, J. M., Gage, K. S., and McIntosh, R. E.: Particle Size Estimation in Ice-Phase Clouds Using Multifrequency Radar Reflectivity Measurements at 95, 33, and 2.8 GHz, *Journal of Applied Meteorology*, 38, 5–28, [https://doi.org/10.1175/1520-0450\(1999\)038<0005:PSEIIP>2.0.CO;2](https://doi.org/10.1175/1520-0450(1999)038<0005:PSEIIP>2.0.CO;2), 1999.
- 5 Simmel, M., Bühl, J., Ansmann, A., and Tegen, I.: Ice phase in altocumulus clouds over Leipzig: remote sensing observations and detailed modeling, *Atmospheric Chemistry and Physics*, 15, 10453–10470, <https://doi.org/10.5194/acp-15-10453-2015>, <http://www.atmos-chem-phys.net/15/10453/2015/>, 2015.
- Sourdeval, O., Gryspeerdt, E., Krämer, M., Goren, T., Delanoë, J., Afchine, A., Hemmer, F., and Quaas, J.: Ice crystal number concentration estimates from lidar–radar satellite remote sensing – Part 1: Method and evaluation, *Atmospheric Chemistry and Physics*, 18, 14327–14350, <https://doi.org/10.5194/acp-18-14327-2018>, <https://www.atmos-chem-phys.net/18/14327/2018/>, 2018.
- 10 Steinhagen, H., Dibbern, J., Engelbart, D., Görsdorf, U., Lehmann, V., Neisser, J., and Neuschaefer, J. W.: Performance of the first European 482 MHz Wind Profiler Radar with RASS under operational conditions, *Meteorologische Zeitschrift*, 7, 248–261, <https://doi.org/10.1127/metz/7/1998/248>, <http://dx.doi.org/10.1127/metz/7/1998/248>, 1998.
- Sullivan, S. C., Hoose, C., and Nenes, A.: Investigating the contribution of secondary ice production to in-cloud ice crystal numbers, *Journal of Geophysical Research: Atmospheres*, 122, 9391–9412, <https://doi.org/10.1002/2017JD026546>, <https://agupubs.onlinelibrary.wiley.com/doi/abs/10.1002/2017JD026546>, 2017.
- 15 Sun, Z. and Shine, K. P.: Studies of the radiative properties of ice and mixed-phase clouds, *Quarterly Journal of the Royal Meteorological Society*, 120, 111–137, <https://doi.org/10.1002/qj.49712051508>, 1994.
- Voigt, C., Schumann, U., Minikin, A., Abdelmonem, A., Afchine, A., Borrmann, S., Boettcher, M., Buchholz, B., Bugliaro, L., Costa, A., Curtius, J., Dollner, M., Dörnbrack, A., Dreiling, V., Ebert, V., Ehrlich, A., Fix, A., Forster, L., Frank, F., Fütterer, D., Giez, A., Graf, 20 K., Groß, J.-U., Groß, S., Heimerl, K., Heinold, B., Häneke, T., Järvinen, E., Jurkat, T., Kaufmann, S., Kenntner, M., Klingebiel, M., Klimach, T., Kohl, R., Krämer, M., Krisna, T. C., Luebke, A., Mayer, B., Mertes, S., Molleker, S., Petzold, A., Pfeilsticker, K., Port, M., Rapp, M., Reutter, P., Rolf, C., Rose, D., Sauer, D., Schäfler, A., Schlage, R., Schnaiter, M., Schneider, J., Spelten, N., Spichtinger, P., Stock, P., Walser, A., Weigel, R., Weinzierl, B., Wendisch, M., Werner, F., Wernli, H., Wirth, M., Zahn, A., Ziereis, H., and Zäger, M.: ML-CIRRUS: The Airborne Experiment on Natural Cirrus and Contrail Cirrus with the High-Altitude Long-Range Research Aircraft HALO, *Bulletin of the American Meteorological Society*, 98, 271–288, <https://doi.org/10.1175/BAMS-D-15-00213.1>, <https://doi.org/10.1175/BAMS-D-15-00213.1>, 2017.
- 25 Westbrook, C. and Illingworth, A.: The formation of ice in a long-lived supercooled layer cloud, *Quarterly Journal of the Royal Meteorological Society*, 139, 2209–2221, 2013.